

Constructing Virtual Representations of Laminated Timber Products

Patrick Grant (✉ p21.grant@qut.edu.au)

Queensland University of Technology

Steven Psaltis

Queensland University of Technology

Maryam Shirmohammadi

Department of Agriculture and Fisheries

Ian Turner

Queensland University of Technology

Research Article

Keywords: Image Analysis, Laminated Timber Products, Engineered Wood Products

Posted Date: September 7th, 2023

DOI: <https://doi.org/10.21203/rs.3.rs-3323846/v1>

License:  This work is licensed under a Creative Commons Attribution 4.0 International License.

[Read Full License](#)

Additional Declarations: No competing interests reported.

Constructing Virtual Representations of Laminated Timber Products

Patrick Grant^{1*}, Steven Psaltis², Maryam Shirmohammadi³,
Ian Turner¹

^{1*}School of Mathematical Sciences, Queensland University of
Technology, 2 George Street, Brisbane, 4000, Queensland, Australia.
²School of Mechanical, Medical and Process Engineering, Queensland
University of Technology, 2 George Street, Brisbane, 4000, Queensland,
Australia.

³Forest Product Innovation, Queensland Department of Agriculture and
Fisheries, 50 Evans Road, Sailsbury, 4107, Queensland, Australia.

*Corresponding author(s). E-mail(s): p21.grant@qut.edu.au;

Abstract

The complex structure of timber has traditionally been difficult to model as it is a highly heterogeneous material. The density (and hence material properties) for structural species such as *Pinus radiata* (radiata pine) can vary greatly across the growth rings. Numerical simulation methods are becoming more prevalent as a method of predicting moisture migration, stress and strain distributions, and fungal/rot intrusion in timber. These methods require a virtual description of an individual board that captures the growth ring structure present in these timbers. In this work, a low-cost algorithm based on image analysis techniques and spectral segmentation is developed for generating a virtual representation of a cross laminated timber panel. The virtual model is generated as a triangular prismatic mesh where the nodes are aligned on the growth rings, with specific wood material properties allocated to each mesh element. The initial step involves identifying the growth ring structure of a single board by analyzing an image of the end grain. The growth rings are then identified using a spectral clustering algorithm. Next, the centre of the tree (pith) is located by using an iterative constrained least-squares algorithm. The density is computed as a proportional length through the growth ring, when provided with an anatomical image of the cellular structure. This density estimate is then assigned to each mesh element.

resulting in the virtual reconstruction of a singular board. Meshes of multiple timber boards are then combined to produce the final mesh of a laminated timber product.

Keywords: Image Analysis, Laminated Timber Products, Engineered Wood Products

1 Introduction

Timber as a construction material provides many benefits over alternatives such as steel, concrete, or clay bricks; it is often cheaper, more sustainable and has comparative strength characteristics (Thomas and Ding, 2018; Abed et al, 2022). This resource is readily available in Australia due to large commercial plantations spread across the country that were estimated to span 1.93 million hectares in 2019 (Downham and Gavran, 2019). The majority of residential buildings in Australia are constructed using timber frames (Navaratnam et al, 2020). Timber can be sawn, peeled and glued into a variety of shapes and sizes. Sawn timber boards are restricted to the size of the tree they are cut from, while engineered wood products (EWPs) made from laminated timbers, which are constructed by gluing boards or peeled surfaces together into a panel, board, or beam, can be fabricated into much greater sizes. Timber production technologies have improved significantly in the past decade and these advancements have led to the construction of multistory buildings using EWPs. There are many types of laminated timbers that are used in construction, with some of the most popular being glued laminated timber (glulam) and cross-laminated timber (CLT), see Figures 1(a) and 1(b) respectively. The tallest building in Australia constructed entirely of laminated timber products, 25 King Street in Fortitude Valley, Queensland, stands 51 meters high and spans 10 floors. The building features a primary support structure made of glulam beams, while its walls and floors are assembled from CLT panels (Wood Solutions, 2022).

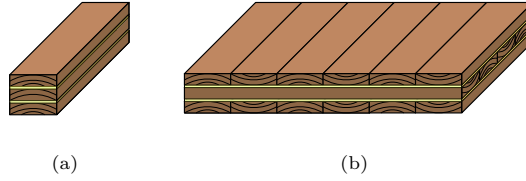


Fig. 1: Illustrative diagram of two laminated timber products. (a) Glulam beam. (b) Cross laminated timber panel (CLT). The yellow regions between the boards indicate the glue lines.

Timber as a material is highly heterogeneous with sharp density changes over the growth rings, making it challenging to model the moisture migration and heat transfer throughout a timber product. The accurate simulation of transport phenomena is important to understand how moisture migration affects the stress and strain characteristics of the complex layered EWPs. The underlying computational model requires the development of a virtual description of an individual board component to be developed, which captures the rapid variation in density evident across the growth rings.

The main aim of this work is to develop a low cost method for generating a complete virtual description of a representative laminated timber product. To achieve this, we start by generating a mesh of a board using a cross-sectional image captured by readily available camera technology. Mathematical tools available in MATLAB ([The Mathworks, Inc., 2022a](#)) are used to identify the timber material property information, such as density variation and grain angle, that is subsequently accommodated in the mesh structure generated using the Gmsh software ([Geuzaine and Remacle, 2009](#)). These individual board components are then assembled into the required laminated timber product.

X-Ray CT is often used in modelling timber as it naturally provides a three-dimensional representation of the material. However, it is not always possible to obtain a CT scan due to maximum size restrictions, cost, or practicality issues. Thus, we

have created a method that uses visible light camera images to generate the mesh structure and a microscope image of the cellular structure to assign a density to each mesh element.

As for all organisms, timber is constructed from cells, the vast majority of which are a certain type of cell called the tracheid (Siau, 1984). Tracheids are long and thin cells with a void space in the centre called the lumen, where water and air can flow. Pits are gaps in the cell wall that allow water and nutrients to travel between cells. Figure 2 depicts how the tracheids are tightly packed in the radial and transverse directions in a section of radiata pine. It should be noted that the longitudinal direction aligns parallel to the centre of the log. In Figure 2, the cell diameters in the transverse direction remain roughly equal between the earlywood and latewood regions, while the cell diameter in the radial direction increases drastically in the earlywood.

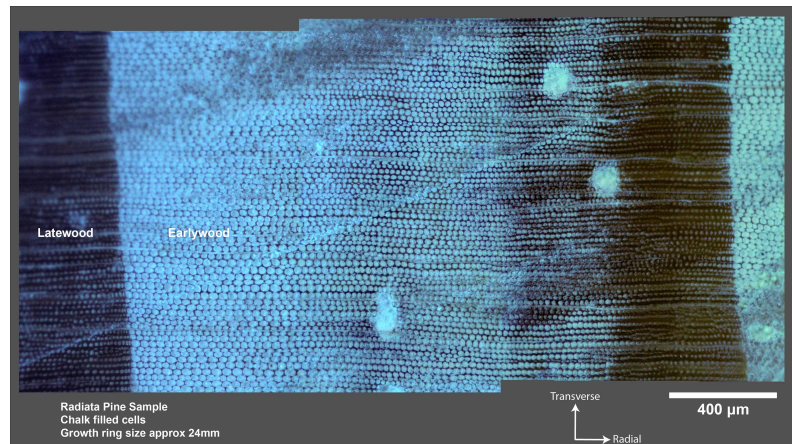


Fig. 2: Anatomical image of a radiata pine cross-section depicting a single growth ring, captured using an optical microscope equipped with a polarizing filter. The image highlights a distinct transition in cell wall thickness observed between the earlywood and latewood regions within the growth rings. Chalk was used to fill any voids within the cells. Image obtained at Queensland Department of Agriculture and Fisheries (QDAF).

As mentioned above, the computational modelling of heat and mass transfer in a timber board requires the use of a mesh, which is a collection of nodes connected together to form elements. These mesh elements can take the form of triangles, and quadrilaterals in two-dimensions, or tetrahedra, triangular prisms, and hexahedra in three-dimensions. For our implementation we use an unstructured two-dimensional triangular mesh that is then extruded longitudinally into a triangular prismatic mesh (see Figure 3). The mesh must be carefully constructed to capture the sharp density variation present across the growth rings within the geometry. To ensure this, it is important that no element lies across the earlywood-latewood boundary as each element will have a unique density associated with it that is computed from the initial image, refer to Section 2.7 where this process is described.

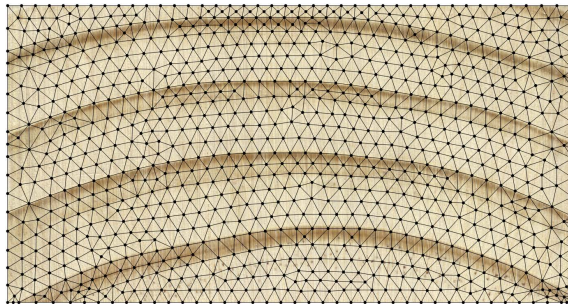


Fig. 3: Example two-dimensional triangular mesh where the nodes (dots) are connected to form triangular elements (lines).

There exist several methodologies for image based mesh generation, however each method is specialised for a given application. Specifically, in the medical industry where three-dimensional data is available from computed tomography (CT) and magnetic resonance imaging (MRI) scanning technologies, Neittaanmaki and others develop a mesh of a human skull (Neittaanmäki et al, 2004). Fang and Boas (Fang and Boas, 2009) generate meshes for a blood vessel network, human brain, and breast tissue from three-dimensional MRI data. Kong and Shadden (Kong et al, 2021) develop a

mesh of a human heart using CT scan data. In the field of wood science, Burridge et al. (Burridge et al, 2021) use 3D X-ray CT scanners to determine the density of the softwood, Sitka spruce (*Picea sitchensis*), and the timber saturation under constant moisture ingress. Acquiring three-dimensional data for timber is feasible but comes with cost and size limitations, making it impractical for general use as it necessitates specialized CT or MRI scanners. Thus, a low cost, accessible method is needed that can generate a two-dimensional mesh from a singular grayscale image, which can then be extruded into the third-dimension.

Perré developed the MeshPore software (Perré, 2005) which allowed the generation of unstructured triangular meshes that align with high contrast features of the input image, either manually or automatically. However, it is worth noting that the software was developed around two decades ago, and its availability may be limited in the present context. Moreover, one limitation of the software was its reliance on high contrast images for optimal automatic mesh generation, which might not always be readily accessible. Figure 4 shows two zones in an end grain image of radiata pine, one with a distinct earlywood-latewood interface and a region where the interface is more ambiguous. There appears to be a research gap in methodologies for identifying the latewood sections of a timber board from an image of the end grain. This work aims to address this growth ring identification problem, which can be effectively divided into two distinct parts. In the first part, image analysis techniques are used to focus on identifying the latewood sections in the end grain image. In the second part, data segmenting is employed to isolate the growth rings from one another, which is a necessary step to construct the two-dimensional triangular mesh.

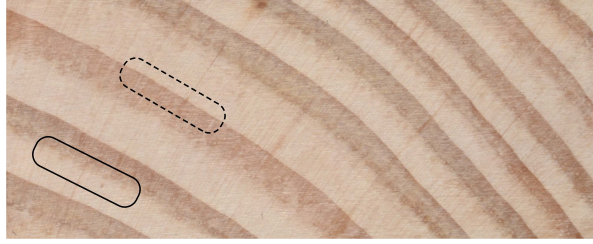


Fig. 4: End grain of a 90mm by 35mm board of radiata pine. The solid black box shows a region where the earlywood-latewood interface is ambiguous while the dashed region shows a distinct boundary between the earlywood and latewood sections.

There are many image analysis methods which can be used to identify image features, including thresholding (Liu et al, 2015), gradient watershed (Gauch, 1999), edge detection (Shrivakshan and Chandrasekar, 2012), and colour feature detection (Gevvers et al, 2006). With such an open ended problem there are likely to be many possible and equally valid methodologies. Following initial investigations into these methodologies, image noise reduction, smoothing and thresholding techniques will be used in this research. The thresholding process results in a binary image mask where each pixel is either a zero or a one depending on the luminance and/or the chrominance of the input image. Each ring needs to be segmented from all the other data points in the mask. Once again there are many methods for segmenting the data such as K-Means clustering (Dehariya et al, 2010), spectral segmentation (Meilă and Shi, 2001), computer vision and machine learning (Liu et al, 2012). A bipartitioning spectral segmentation algorithm was developed to segment the image mask. The details of which are presented in Section 2, where we also present the methodology used for generating an individual virtual board. This includes mesh generation, a pith locating algorithm, mesh density computation and the determination of the equilibrium moisture content. Multiple boards are combined to construct the virtual laminated timber product presented in Section 3. Following this is a discussion of the pros and cons of the developed method in Section 4. The conclusions of the work are then summarized in section 5.

2 Methodology

The proposed methodology for generating the virtual description of a laminated timber product can be summarized as follows. A photograph or a scan of the end grain pattern serves as the starting point for generating the mesh. Initially, an unstructured two-dimensional mesh is generated using the end grain image, which is then extruded into the longitudinal direction using triangular prismatic mesh elements. Finally, the meshes of multiple boards are combined to create the mesh for a laminated timber product. The majority of the code is written in MATLAB, and Gmsh is used to mesh the geometry specified by the MATLAB codes. All code and supporting files are uploaded to the following GITHUB repository: <https://github.com/psgrant/TimberMeshGen>.

2.1 Timber Imaging

The process of mesh generation commences with the capture of an image of the end grain of a timber board. As mentioned in the introduction, one of the requirements of our modelling strategy is to use readily available, inexpensive equipment and we have found that either a digital single lens reflex (DSLR) camera or a flatbed scanner were suitable for this task. Our extensive testing indicated that the use of a scanner typically produced more reliable results with less image processing required however, the board must be small enough to be scanned. Although the DSLR camera was not as effective as the scanner, we found it much easier and faster to obtain images. However, positioning the camera close to the board resulted in the image being warped due to the ends of the board being further away from the camera. We were able to optimise the image quality using a lens with a longer focal length ($> 100\text{mm}$ full frame equivalent) positioned further away from the board. This is conceptualised in Figure 5. Using a scanner negates this issue as all the scan head moves in parallel with the board.

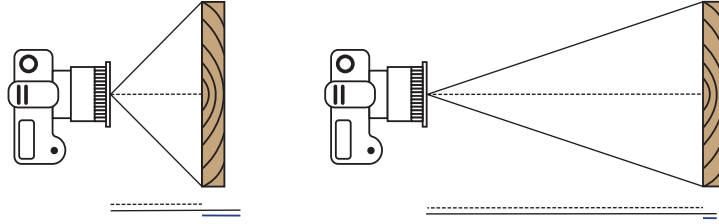


Fig. 5: Diagram depicting the warping due to the camera being closer to the timber board. The bottom line represents the difference in lengths between the center (dashed) line and the edge (solid) lines.

2.2 Image masking

Once a suitable image is obtained it is converted to grayscale and the size of the image is reduced. Next, a Gaussian blur is applied to the image to reduce high fidelity noise. Then a mask is defined as a logical array having the same size as the image. The mask contains either zeros or ones, a one indicates pixels in the darker latewood sections and a zero indicates pixels in the earlywood, refer Figure 6. The generation of the mask involves three main steps: Gaussian filtering, brightness thresholding, and median filtering. After the Gaussian filtering, the user selects a specific brightness threshold during the brightness thresholding stage, where pixels darker than the threshold are marked. Finally, the median filtering step is performed to remove small clusters of marked points that do not correspond to the latewood region.

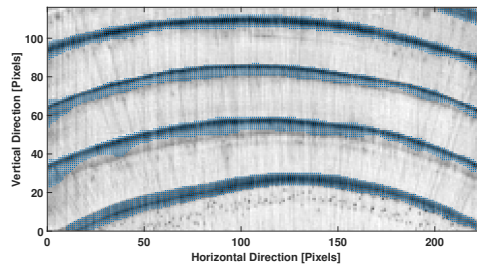


Fig. 6: Example image mask of a reduce size image where the blue dots highlight the flagged pixels in the image mask.

2.3 Spectral Segmentation

Once the image mask has been generated and filtered, the spectral segmentation can commence. This algorithm is desirable as it is a high performance data segmenting algorithm where orientation does not matter (Cour et al, 2005). The process begins with the generation of a similarity matrix $\mathbf{W} \in \mathbb{R}^{n \times n}$ where n is the number of points to be segmented (Von Luxburg, 2007). The entries in the similarity matrix can be constructed to take into consideration different data property features, some examples include: spatial distance, pixel colour, pixel light intensity (Jia et al, 2014). For our implementation we have used physical distance between the points in the image mask. The graph Laplacian, $\mathbf{L} \in \mathbb{R}^{n \times n}$, is then generated as:

$$\mathbf{L} = \mathbf{D} - \mathbf{W},$$

where $\mathbf{D} \in \mathbb{R}^{n \times n}$ is the diagonal matrix,

$$\mathbf{D}_{ii} = \sum_{j=1}^n \mathbf{W}_{ij}, \quad i = 1, \dots, n.$$

The elements of \mathbf{W} are computed as a Gaussian weighted spatial distance between each point pair in the data set,

$$\mathbf{W}_{ij} = \exp \left[-\frac{\|\mathbf{x}_i - \mathbf{x}_j\|_2^2}{2\sigma^2} \right], \quad (1)$$

where \mathbf{x}_i and \mathbf{x}_j are the i th and j th position vectors in the image mask respectively and σ is a parameter which controls the size of the point neighborhoods.

The eigenvalues and eigenvectors of the graph Laplacian, \mathbf{L} , are computed and sorted in ascending order. The signs of the elements in the eigenvector that corresponds to the second smallest eigenvalue (Fiedler vector) designate which bipartition that point is in, see Figure 7(a). The second vector is chosen as the elements in the first eigenvector are all constant with a value of $1/\sqrt{N}$, where N is the number of points

to be bipartitioned. This process is repeated until all data sets are segmented. The outcome is exhibited in Figure 7(b).

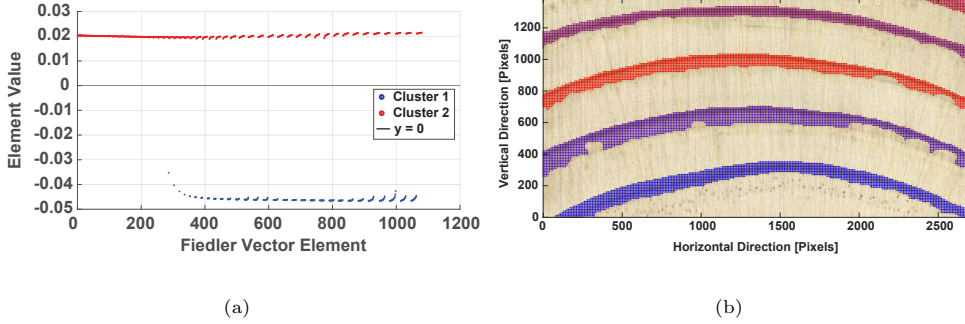


Fig. 7: (a) Example Fiedler vector values. (b) Final result of clustering where each segment is a different colour.

Notice that there are partially incomplete regions evident in the image mask, on the bottom side of the two central growth rings in Figure 7(b). These regions form as a result of the latewood section not being as dark in these sections and thus, weren't captured in the thresholding stage. These incomplete regions can be filled by fitting a boundary around the points in each newly segmented growth ring, illustrated in Figure 8. The boundaries are computed using the inbuilt MATLAB function: `boundary` (Mathworks, Inc., 2022), which takes the x and y positions of each point and a shrink factor parameter $0 \leq S \leq 1$ as inputs. MATLAB's `boundary` function generates an alpha shape which returns a triangulation that encloses a set of data points when given a radius, α (Edelsbrunner and Mücke, 1994). The α radius is directly correlated to the shrink factor, S , in the `boundary` function. When $S = 0$ the boundary is the convex hull of the data points, and $S = 1$ generates the tightest single region boundary around the points. As the shrink factor decreases from one to zero the boundary becomes less compact. The boundaries depicted in Figure 8 use a shrink factor of $S = 0.15$. During testing it was found that this choice of shrink parameter is ideal as it follows the edges of the growth rings closely and bridges the gaps evident in the

incomplete regions identified in Figure 7(b). Larger values of S result in the boundary not filling these regions and smaller values start filling in too much as the boundary approaches the convex hull. The area enclosed by these boundaries is then filled with data points and these new regions are used when fitting the smoothing splines for the earlywood-latewood boundaries that will be outlined in Section 2.4.

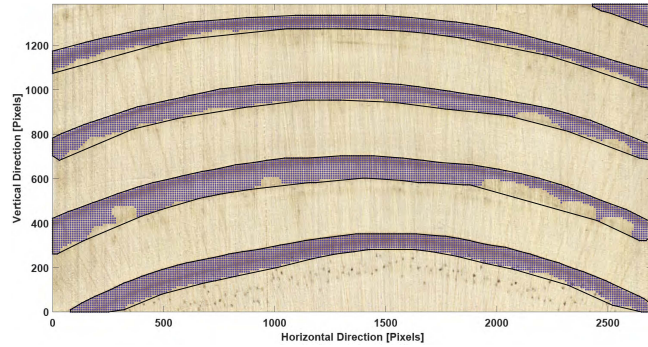


Fig. 8: Boundaries determined using MATLAB's `boundary` function, with shrink factor $S = 0.15$.

To determine if a bipartition (cut) is optimal, we check if the boundary elements of each data set lie directly adjacent to each other. This way we ensure that each segment contains only one growth ring. The left side of Figure 9 presents an example of a suboptimal bipartition. In panels A and B, observe that the boundary points of the two clusters (black circles) are next to each other. An optimal cut is achieved by reducing the σ parameter thus obtaining a different cut as depicted in panels C and D. The right side of Figure 9 presents an optimal cut.

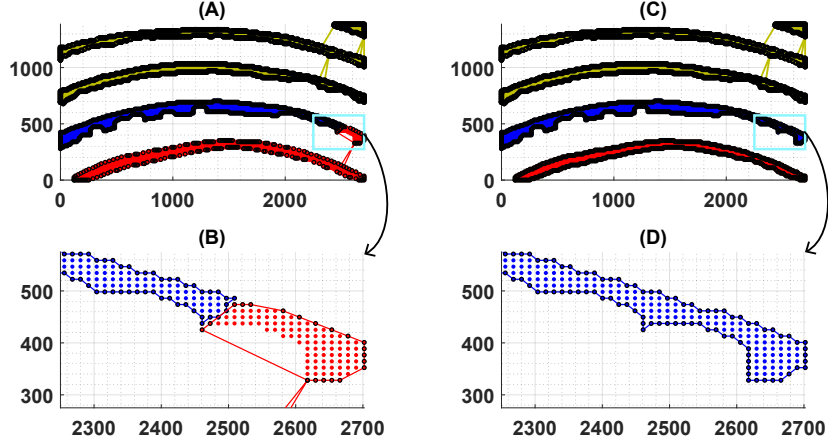


Fig. 9: Example bipartitions, where the yellow regions represent already-segmented growth rings, and the red and blue regions indicate the bipartitions currently under consideration. Panels A and B illustrate suboptimal cuts, which involve cutting through a growth ring. Panels C and D show optimal cuts with reduced σ , which involve segmenting the entire growth ring.

A parameter sweep was conducted for the value of σ given in (1), which controls the size of the point neighborhoods, over the interval $[1.5, 8]$ with a resolution of 0.01. The three sample images depicted in Figure 10, resulting from different sawing patterns, were tested using the algorithm described above. These different samples, referred to as quartersawn, plainsawn, and backsawn, have image sizes of 3134×1262 , 410×410 , and 2702×1385 pixels respectively. Initially the σ parameter was held constant throughout the whole process and if a single iteration did not result in an optimal bipartition then the algorithm was deemed a failure for that value of σ . Convergence of the algorithm is considered successful if the same constant value of σ could be applied throughout the iterative bipartitioning process to identify all growth rings within the image. In Figure 11(a) we show the regions of convergence coloured in blue for each of the sample images. The regions where convergence could not be achieved are coloured in pink. The convergence regions appear quite similar for the quartersawn and backsawn images, approximately $3.4 \leq \sigma \leq 4.4$. However convergence is poor for the plainsawn

image. This is possibly due to the smaller image size of the plainsawn image, thus resulting in smaller distance between points in the image mask.

The uncertainty in the parameter choice is reduced by introducing an adaptive parameter updating scheme. If the bipartition results in a suboptimal cut σ is reduced by 0.1 until it reaches the lower threshold of 0.1, after which it is increased to $\sigma = 8$ and the process is repeated. From Figure 11(b) it can be seen that any value of $3.4 \leq \sigma \leq 8$ converged for the three images using the parameter updating scheme. Observe the large gray regions to the right of the blue regions in all three samples, that arise because the parameter value has been iterated down to a value that is able to converge.

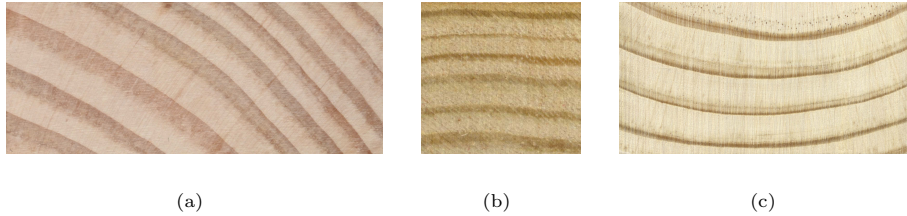
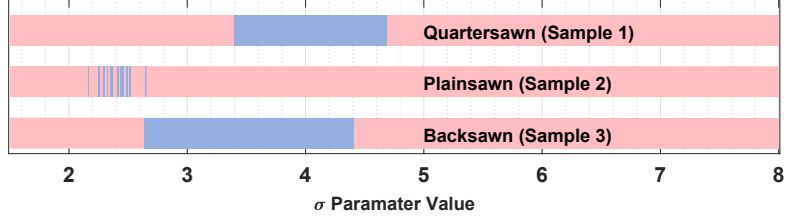
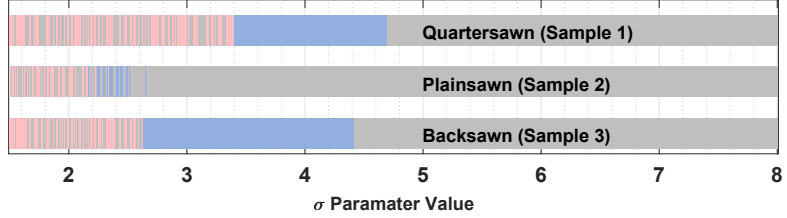


Fig. 10: Three test samples used for σ parameter sweep. (a) 90mm×35mm quarter-sawn board. (b) 20mm×20mm plainsawn board. (c) 90mm×45mm quartersawn board.



(a)



(b)

Fig. 11: Parameter sweep of the Gaussian weighting parameter, σ , in Equation (1) where the pink sections indicate regions of no convergence, the blue regions indicate that the algorithm was able to successfully converge using the same σ value for all iterations and the gray regions indicate convergence where σ was updated. (a) Initial parameter sweep holding σ constant. (b) Iterative σ algorithm.

Interestingly the quartersawn and backsawn boards both have similar regions of convergence and the plainsawn board had only a few values of σ that resulted in the algorithm converging. The recommended approach is to select a higher initial value for σ (the value $\sigma = 6$ proved effective during testing). Although this may increase the runtime, it enhances the likelihood of achieving convergence towards a solution. For values of $\sigma < 2.5$ there appears to be a region of instability for convergence in Figure 11(b). As σ decreases, the graph Laplacian, \mathbf{L} , becomes more sparsely populated with information having narrower Gaussian weighting, meaning there is less connectivity information available.

2.4 Determining the Earlywood-Latewood Boundaries

The points on the outside boundary of each growth ring section are found using the previously mentioned `boundary` function with $S = 1$, to ensure the tightest single region boundary is identified. The boundary points above and below the latewood sections are then isolated and a cubic smoothing spline fitted through the boundaries. The result of this process is shown in Figure 12.

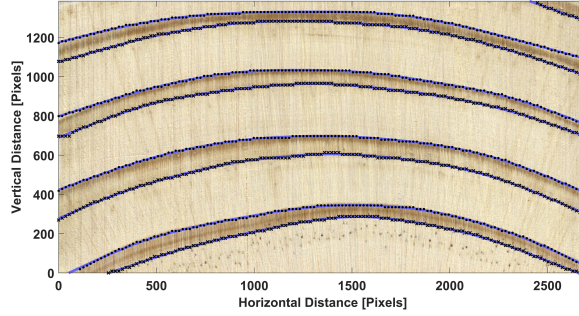


Fig. 12: Fitted cubic smoothing splines through the earlywood-latewood boundaries.

The piecewise cubic smoothing spline $f(x)$, over the interval $x \in [a, b]$, with smoothing parameter $p \in [0, 1]$ minimizes (De Boor and De Boor, 1978) the following expression:

$$p \underbrace{\sum_{i=1}^n |y_i - f(x_i)|^2}_{\text{Least Squares Term}} + (1-p) \underbrace{\int_a^b \left(\frac{d^2 f}{dx^2} \right)^2 dx}_{\text{Roughness Penalty}},$$

where each cubic subsection of the piecewise smoothing spline is denoted by x_i , and n is the number these cubic subsections. The first term is a standard least squares minimization and the second term is a roughness penalising term. When $p = 1$ the smoothing spline simply interpolates all the data points, when $p = 0$ the minimization problem reduces to a linear least squares estimate. For intermediate values the smoothing spline lies somewhere between the piecewise smooth cubic interpolation and the linear least squares estimate (De Boor and De Boor, 1978). Reinsch (Reinsch,

1967) recommends a value of $p = 1/(1 + h^3/6)$, where h is the average spacing of the data. MATLAB's curve fitting toolbox is used to generate and evaluate the splines (The Mathworks, Inc., 2022b).

2.5 Generating the Computational Mesh

The benefit of using splines is that they are defined over the whole domain. They also smooth out the noise inherited from the image masking process in the input data, providing a more realistic fit to the growth ring boundaries. Next, we need to generate the mesh (using Gmsh) from the fitted smoothing splines. It is important that there only exists one material type in each element, either the earlywood or latewood. By placing the nodes of the mesh on the growth ring boundaries it ensures that the triangular elements will not cross the boundary. For the mesh generation, we are only interested in the latewood to earlywood (from the pith, discussed in subsection 2.6) spline as that is where the sharp density variation is present. Control over the mesh refinement is also required, especially on the edges of the board and along the internal growth ring boundaries. Mesh refinement will be controlled by specifying the number of nodes along these splines, achieved defining the splines as Transfinite curve type in Gmsh. The process of mesh generation commences with the construction of smaller rectangular boxes where the mesh refinement will be specified within that box. Figure 13 demonstrates how each part of the splines pass through each box. Careful consideration has been given to where the curves briefly enter a zone and leave quickly. For these scenarios, the refinement of the previous box is applied, refer to the top right corners of the two internal boxes in Figure 13.

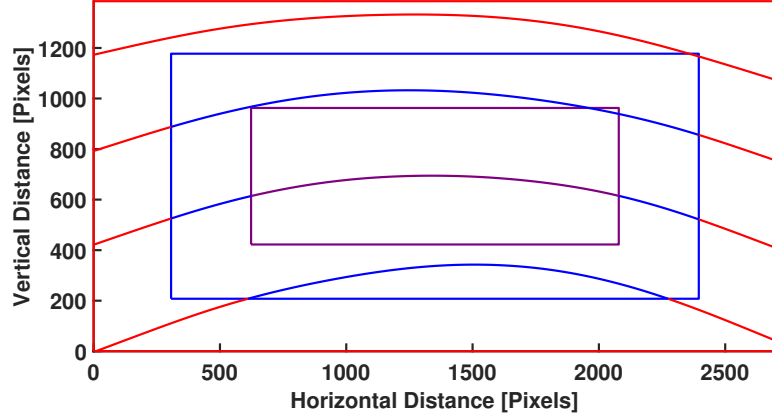


Fig. 13: Example geometry refinement zones with two internal boxes. It can be observed that the splines that only slightly extend into the top right corner of the internal boxes do not undergo any refinement changes.

Gmsh is an open source meshing software package that provides the user with many powerful tools for mesh generation (Geuzaine and Remacle, 2009). The user defines the geometry of the object to be meshed alongside the desired level of refinement, then Gmsh will generate the mesh for that geometry and refinement. The meshes can be one-, two- or three-dimensional and consist of many element types, for example: triangular, quadrilateral, tetrahedra, triangular prism, etc. The strategy we adopt is to generate a two-dimensional unstructured triangular mesh that describes the growth ring variation in the RT cross section, then extrude the mesh (in the longitudinal direction) to produce a three-dimensional triangular prismatic mesh. The splines that pass through different refinement zones get split into multiple smaller sub-splines, one for each zone. Gmsh handles mesh refinement in several ways however it was found that defining the number of nodes desired along each sub-spline produced suitable meshes. The length of each segment is computed and the corresponding node count applied. For example, if a sub-spline is 283 pixels long and is in the 25 pixels per node (PPN) section then there would be 11 nodes along that segment (including the two

end nodes). Figure 14 displays a mesh that is refined more towards the edges of the domain, showing that a higher PPN results in a coarser mesh.

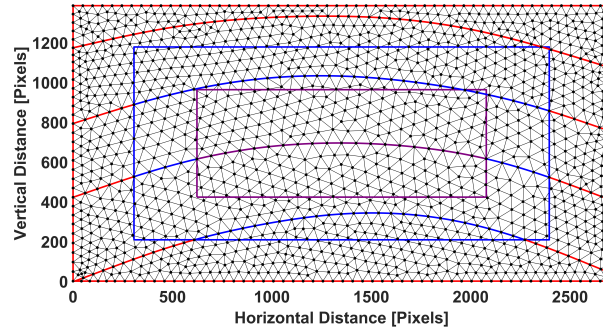


Fig. 14: Example mesh with three refinement zones, starting with 50 pixels per node (PPN) in the red zone, 60 PPN in the blue zone and 70 PPN in the purple zone.

Using the `extrude` function within Gmsh the two-dimensional mesh can easily be extended into the longitudinal dimension. Figure 15 depicts the mesh generated in Figure 14 extruded with 21 layers (including the initial two-dimensional mesh). It is important to note that the number of layers desired does not include the initial mesh. Gmsh can export the mesh data in many widely used formats, in our implementation we export the mesh data as a MATLAB script file.

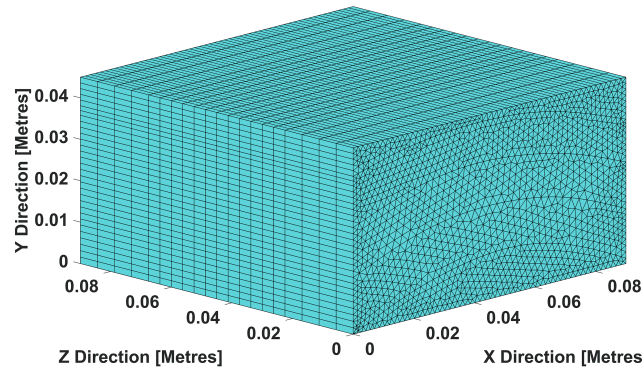


Fig. 15: Example three-dimensional triangular prism mesh with 21 non-uniformly distributed layers.

2.6 Pith Locating Algorithm and Grain Angle Computation

Material properties are defined in the radial, transverse and longitudinal directions of the timber board (Perré and Turner, 2001). Thus a standard transformation matrix must be applied to the material properties to obtain the material properties in the x , y and z directions. To illustrate, we exhibit how this rotation matrix, \mathbf{R} , is applied to the effective thermal conductivity $\tilde{\mathbf{K}}_{\text{eff}}$ tensor:

$$\mathbf{R} = \begin{pmatrix} \cos \theta & -\sin \theta & 0 \\ \sin \theta & \cos \theta & 0 \\ 0 & 0 & 1 \end{pmatrix}, \quad \tilde{\mathbf{K}}_{\text{eff}} = \begin{pmatrix} K_{\text{eff}}^R & 0 & 0 \\ 0 & K_{\text{eff}}^T & 0 \\ 0 & 0 & K_{\text{eff}}^L \end{pmatrix},$$

where θ is the grain angle, K_{eff}^R , K_{eff}^T and K_{eff}^L are the effective thermal conductivities in the radial, transverse and longitudinal directions respectively. The rotated effective thermal conductivity tensor is then expressed as follows:

$$\mathbf{K}_{\text{eff}} = \mathbf{R}^T \tilde{\mathbf{K}}_{\text{eff}} \mathbf{R}.$$

The grain angle is defined as the angle of the board from the horizontal axis from the pith, refer Figure 16(a).

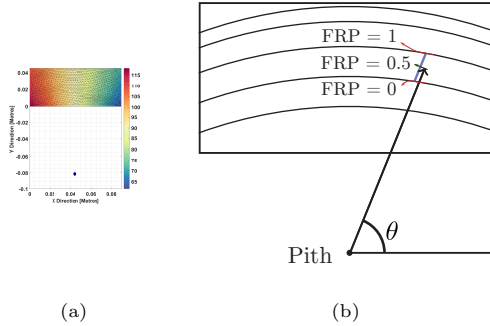


Fig. 16: (a) Description of the grain angle θ , where R and T represent the radial and transverse directions respectively. (b) Visual description of the fractional radial position (FRP) which is a relative measure of how far a point is through a given growth ring.

To determine the grain angle for each node in the mesh, it is necessary to estimate the location of the pith. To do this, we sample points from the cubic smoothing splines previously presented in Section 2.4 and fit a circle through each spline, fitting for the radius and the center of the circle. Consider the equation for a circle centred at (x_0, y_0) with radius R :

$$(x - x_0)^2 + (y - y_0)^2 = R^2,$$

which can be expressed as:

$$x^2 + y^2 = R^2 + 2xx_0 + 2yy_0 - x_0^2 - y_0^2,$$

then the subsidiary coefficients can be absorbed into a new variable $A = R^2 - x_0^2 - y_0^2$, to give

$$x^2 + y^2 = A^2 + 2xx_0 + 2yy_0. \quad (2)$$

By computing a least squares fit on Equation (2) the coefficients A, x_0 and y_0 can be found. The radius can be recovered with:

$$R = \sqrt{A + x_0^2 + y_0^2}.$$

The process is performed twice for each growth ring to determine the pith location and radius for the two borders of the latewood section. This yields a set of potential pith locations and radii. In the subsequent iteration, we recalculate the least squares fit, constraining the pith locations within a box with a height and width that equals half of the standard deviation of the circle centers from the previous iteration, see A. Figure 17(a) presents the approximate pith location for a backsawn timber board of radiata pine after 15 iterations. This method allows for an approximate pith location to be found, and then be used to compute the grain angle of a given board. With the

pith location computed, the grain angle can be found for each element and node of the mesh, refer Figure 17(b). This allows the material properties that are computed in the radial, transverse and longitudinal directions to be represented using the x , y and z directions.

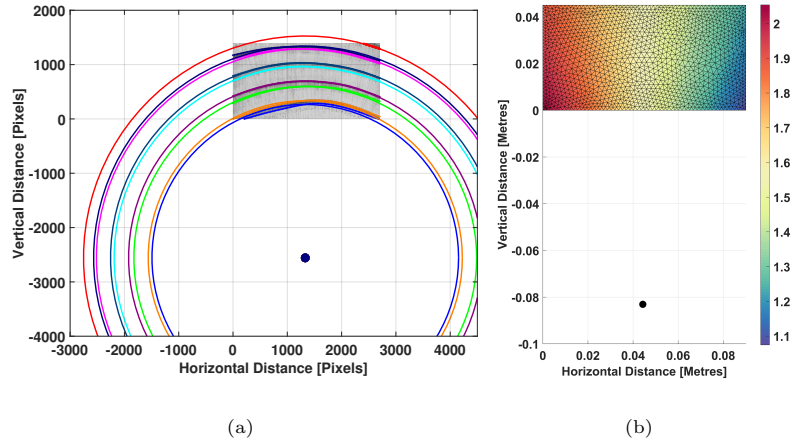


Fig. 17: (a) Fitted circles through the earlywood-latewood interface with an approximate pith location shown as the black dot, measured in pixels. (b) The grain angle (radians), θ , of the backsawn board.

Recent publications have used a similar approach to locate the pith of Norway spruce timber (Habite et al, 2020), to achieve good estimations of the pith locations and average annual growth rate (growth ring width). They assumed that the growth ring width is constant throughout the whole board, which for Norway spruce was a valid assumption. This assumption breaks down when considering timber species with non-uniform growth ring widths and spacing, such as radiata pine. The method presented in this article allows for varying growth ring sizes as each earlywood-latewood boundary is considered independently, instead of treating the latewood section of the growth ring as one entity.

2.7 Mesh Density

Computed tomography (CT) and magnetic resonance imaging (MRI) scanners have been demonstrated to generate 3D profiles of timber density and moisture (Burrige et al, 2021; Lazarescu et al, 2010), however, the requirement for isolated timber sections, together with the need for specialized training and expensive equipment make their practical usage challenging. We propose a method for determining local density values by computing the intra-growth ring fractional radial position (FRP) across the board. Then, a five-point logistic function is used to relate density to the FRP, where the data for the fit is obtained by multiplying the surface fraction of the cell wall by its density (Perré, 1997). Lastly, each element in the two-dimensional triangular mesh is assigned a constant density value, which is then used for all triangular prismatic elements emanating from that triangular face extruded into the longitudinal direction.

To determine local density, the first step is to identify which growth ring boundaries the centroid of each mesh element lies between. We only need to consider the latewood to earlywood boundary (from the pith) as that is where the sharp change in density exists. Next, the FRP is computed by seeing how far through a given growth ring each element centroid, depicted in Figure 16(b). The FRP is used as the absolute distance between each growth ring, and scaling the distances between zero and one allows the density to be easily computed by applying the five-point logistic function that is defined over the domain $[0,1]$. The splines are extended outside the board boundaries so that the distance for points on the edge can still be computed.

For regions where there is no spline between the pith and the element, (regions labelled zero) in Figure 18(a), we use the next growth ring (regions labelled one) splines. The idea is to project back those splines and compute the FRP as if the element were between those two splines. Similarly this idea is applied to elements where is no spline that intersects the pith-element ray after the element (regions labelled four), however we project forward the splines from the previous zone (regions labelled three).

This process enables the centroid of each mesh element to have assigned a FRP along the growth ring.

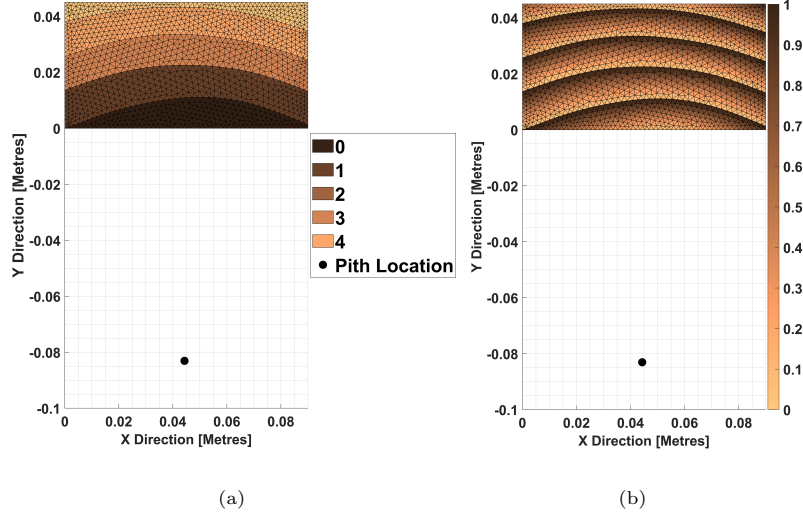


Fig. 18: (a) Regions which indicate how many growth rings a ray has passed through. (b) The fractional radial position across the whole board.

Next the five-point logistic (5PL) function is used to convert the FRP to a density value for each element. Each parameter in the 5PL function has a distinct physical characteristic that affects the shape of the curve, where the five-point logistic function is defined as:

$$\rho(x) = \beta_0 + \frac{\beta_1 - \beta_0}{\left(1 + \left(\frac{x}{\beta_2}\right)^{\beta_3}\right)^{\beta_4}}, \quad (3)$$

where ρ is the density, x is the fractional radial position, β_0 and β_1 are the minimum and maximum densities respectively, β_2 is the inflection point (when $\beta_4 = 1$), β_3 is the slope factor which describes the steepness of the curve and β_4 is an asymmetry coefficient (Psaltis et al, 2021). The 5PL is often used in many biological applications where growth is concerned (Koya and Goshu, 2013) and has previously been used

for fitting the modulus of elasticity in timber (Psaltis et al, 2021). We extend its application to fitting the density of radiata pine to the FRP.

The radial density can be computed using image analysis on an anatomical image of timber acquired at the Queensland Department of Agriculture and Fisheries experimental facility located at Salisbury in Brisbane, using the method described in (Perré, 1997). The image is thresholded so the cell wall pixels are masked, then divided into vertical strips and the proportion of the strip that is the cell wall can be computed. This proportion is then multiplied by the solid phase density of timber, $\rho_s = 1530 \text{ kg m}^{-3}$. The width of the image encompasses a single growth ring, the x -coordinate data is then rescaled to be between zero and one, which is fitted using the 5PL function. Table 1 presents the coefficients along with the upper and lower bounds placed on these coefficients determined by completing a constrained least-squares fit using MATLAB’s Curve fitting toolbox (The Mathworks, Inc., 2022b). The FRP, depicted in Figure 19 is then used to assign a density for each mesh element.

Table 1: Fitted parameter values for the five-point logistic function described in Equation (3).

Coefficient	Value	Lower Bound	Upper Bound
β_0	573.3	400	1000
β_1	262	0	400
β_2	1.1	0	2
β_3	5.1	0	10
β_4	9.8	0	10

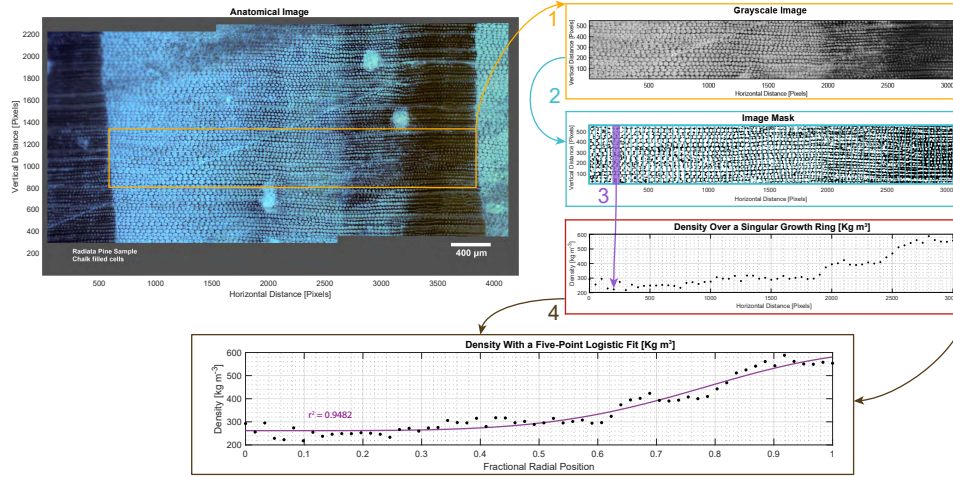


Fig. 19: The flowchart illustrates the process for determining density values within a single growth ring. The four main steps, indicated by arrows and corresponding step numbers, are: 1) selection of the desired region and conversion to grayscale, 2) application of an image mask to identify the cell wall pixels using MATLAB's `adaptthresh` function, 3) calculation of the proportion of black pixels within each column and multiplication by a solid density ρ_s , 4) normalisation of horizontal pixel distance to a fractional radial position and fitting of a five-point logistic function.

Figure 20(a) shows an example where each mesh element is assigned a density as computed from the 5PL. This can then be extruded from the two-dimensional triangular mesh into a three-dimensional triangular prismatic mesh, as shown in Figure 20(b).

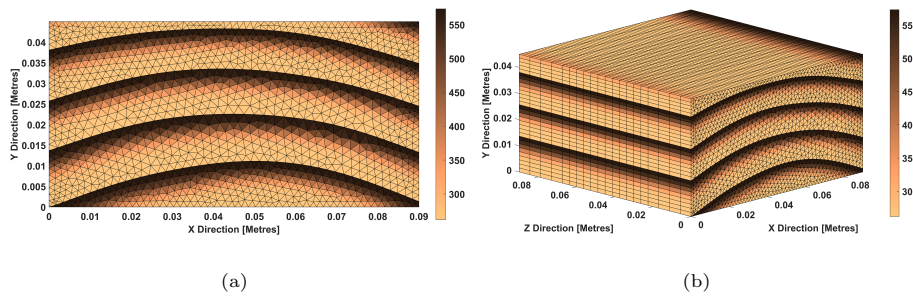


Fig. 20: (a) Two-dimensional mesh populated with density values. (b) Extruded three-dimensional mesh.

2.8 Equilibrium Moisture Distribution

With the virtual representation now constructed, we can compute the equilibrium moisture distribution which is often used as the initial condition for numerical simulation of heat and mass transfer. The equilibrium moisture distribution is determined for moisture contents exceeding the fibre saturation point (FSP) and when the capillary pressures throughout the timber board are in equilibrium (Perre and Turner, 2002). The local capillary pressure, $P_c(S_w^{(i)}, \rho_0^{(i)}, T)$, is defined in terms of the free water saturation, density and the temperature and its functional form is described in (Perré and Turner, 2001). When the average moisture content of the whole board, \bar{X} is below the FSP the moisture content throughout the board is assumed constant at that value. To compute the moisture distribution, the averaged timber density at each node is required and we construct control volumes around each node in a vertex-centred manner, as demonstrated in (Carr et al, 2011). The average density $\rho_0^{(i)}$ defined at each node i is described as follows:

$$\rho_0^{(i)} = \frac{\sum_{j=1}^m \rho_0^{(j)} A_j}{\sum_{j=1}^m A_j},$$

where m is the number of elements that surround node i , $\rho_0^{(j)}$ is the density that associated with element j and A_j is the area of the sub-control volume in element j . The initial moisture distribution is determined by solving a system of nonlinear equations that enforces the equilibrium of the capillary forces and an overall mass balance throughout the domain (Perre and Turner, 2002). This system is given as follows:

$$f_i(\mathbf{s}) = P_c(S_w^{(i)}, \rho_0^{(i)}, T) - P_c^{\text{eqm}}, \quad i = 1, 2, \dots, N$$

$$f_{N+1}(\mathbf{s}) = \rho_w \frac{\sum_{i=1}^N \phi^{(i)} S_w^{(i)} A_i}{\sum_{i=1}^N \rho_0^{(i)} A_i} - X_{\text{FSP}} - \bar{X},$$

where N is the number of nodes, $\mathbf{s} = (S_w^{(1)}, S_w^{(2)}, \dots, S_w^{(N)}, P_c^{\text{eqm}})^T$ is the solution vector containing the free water saturation values at each node and the equilibrium capillary pressure, $\phi^{(i)}$ is the nodal porosity, A_i is the control volume area of node i , P_c^{eqm} is the equilibrium capillary pressure and \bar{X} is the averaged moisture content of the entire board. The fibre saturation point, X_{FSP} , linearly decreases with temperature as given by $X_{\text{FSP}} = 0.325 - 0.001T$ (Stamm, 1961). The nodal moisture content is computed from the free liquid saturation, $S_w^{(i)}$:

$$X^{(i)} = \frac{\phi^{(i)} S_w^{(i)} \rho_w}{\rho_0^{(i)}} + X_{\text{FSP}}, \quad \phi^{(i)} = 1 - \rho_0^{(i)} / \rho_s.$$

where ρ_w is the density of water. The resulting nonlinear system can be solved with an iterative solver such as an inexact Newton solver using first order finite difference approximations for the terms in the Jacobian matrix (Burden et al, 2015). The initial condition for the Newton solver is simply that every node has a constant value of \bar{X} . An example three-dimensional moisture profile for a CLT panel section with $\bar{X} = 1$ kg(water)/kg(dry solids) is presented in Figure 21(c).

3 Results

The combination of the methodologies described in the previous section allows for the generation of a virtual three-dimensional representation of a timber board, which can be used to simulate moisture migration and heat transfer. The mesh contains information on density and grain angle which enable the calculation of material properties for the timber board and computation of the equilibrium moisture profile. By treating each board individually and combining each component together, a virtual laminated timber product can be created. Figures 21(a), 21(b), and 21(c) illustrate a typical example of a three-layer cross-laminated timber panel section, along with the computed elementwise density, and equilibrium moisture distribution respectively. We see that the moisture distribution tends to follow the density variation, pooling in the less

dense, earlywood regions. From this it is easy to see the lack of longitudinal variation throughout the CLT panel section.

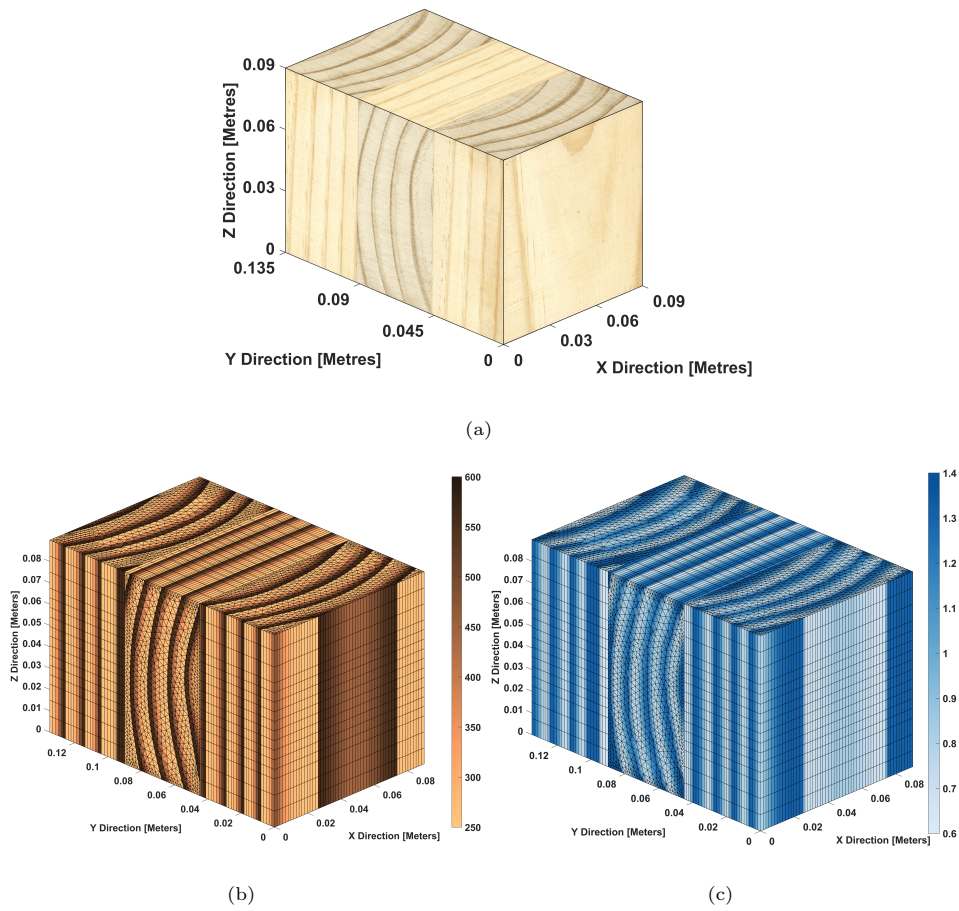


Fig. 21: (a) Texture mapped surface of a 3 board cross-laminated timber panel. (b) Elementwise density of the CLT panel. (c) Nodal equilibrium moisture distribution.

4 Discussion

The aim of this research is to develop a low-cost method for generating virtual representations of laminated timber products, capturing the sharp density variation across

the growth rings within the mesh geometry. By combining well-established image analysis techniques, linear algebra, and spectral clustering algorithms, three-dimensional reconstructions of laminated timber products can be achieved. The proposed low-cost method provides the user with an acceptable virtual reconstructions of laminated timber products which requires a grayscale image of the end grain of the timber boards and an anatomical image as inputs. Where the end grain image is used to generate the mesh and for locating the pith, and the anatomical image is used for assigning a density to each mesh element. However, it should be noted that the current method, which involves generating a two-dimensional triangular mesh and extruding it into a three-dimensional triangular prismatic mesh, results in the loss of information along the longitudinal direction. When considering these smaller samples, the variation in the longitudinal direction is minimal. This limitation arises from the assumption that the growth ring patterns do not vary longitudinally, which is a reasonable assumption given the constraints of working with a single image and the loss of access to the sides of the boards during lamination. Overcoming this challenge and developing a method that incorporates longitudinal variation into the three-dimensional mesh formation process is non-trivial.

There also appears to be limited literature regarding automated algorithms for locating the pith when only given an image of the end grain of a timber board. Habite, et al. (Habite et al, 2020, 2022) used two neural networks to locate the pith of Norway spruce (*Picea abies*) timber boards to great success. The first used a conditional generative adversarial network (cGAN) (Habite et al, 2020), and the latter used a one-dimensional convolutional neural network (Habite et al, 2022). Moreover, it is difficult to estimate the location of the pith using the plastic sheet of concentric circles described by Habite, et al's (Habite et al, 2022, 2020). Some other work by Briggert, et al. (Briggert et al, 2016) used tracheid-effect scanning to determine the fibre orientation to model the shape of knots and to locate the pith for Norway spruce. We believe

the iterative pith location algorithm developed in Section 2.6 offers a new contribution in this research field and is able to produce plausible pith locations that accounts for irregular growth ring widths and spacings exhibited in radiata pine (Kadas, 2016).

5 Conclusion

This work presents a comprehensive procedure for generating detailed virtual representations of laminated timber products. The method utilizes techniques from image analysis and spectral segmentation to generate a two-dimensional unstructured triangular mesh where the elements are aligned along the growth rings. The pith is then located using an interactive constrained least-squares algorithm. Each element can be assigned a density based on its relative position inside a growth ring using a five-point logistic function fitted from data obtained from a microscope image. This density variation facilitates the determination of the equilibrium moisture content. Three-dimensional meshes are generated by propagating the two-dimensional triangular meshes into triangular prismatic meshes, along with the extrusion of the density and moisture information. Lastly, multiple boards can be combined to reconstruct the laminated timber. The main findings of this study were:

- By combining Gaussian filtering, brightness thresholding, and median filtering as image analysis techniques, an image mask can be generated to highlight the latewood sections of the growth rings.
- The spectral segmentation algorithm performs excellently in segmenting the rings within the image mask. Moreover, the algorithm's performance remains unaffected by the orientation of the board or the type of sawing pattern.
- Using an iterative constrained least-squares algorithm that fits circles for each growth ring, the pith can be accurately located.
- To compute the density across the growth ring, the five-point logistic function is fitted against data obtained from an anatomical image.

- The developed method produces three-dimensional virtual representations of laminated timber products, including density variation and the initial moisture distribution.

The method developed in this study has shown great promise in generating a computational mesh that accurately represents the sharp change in density across the growth rings of laminated timber products constructed on radiata pine. The use of image analysis techniques and spectral segmentation is a low-cost approach, making it an attractive alternative to other more expensive and time consuming methods such as X-Ray CT scanning. However, it is important to note that this method has its limitations. As it only uses images from the end grain, information in the longitudinal direction can not be recovered. This means that the computational mesh generated by this method will not provide a complete representation of the material variation in the longitudinal direction internal structure. The virtual representation serves as a foundational platform for future research, allowing for the accurate simulation of heat and mass transfer within these laminated timber products. Additionally, by coupling the heat and mass transfer model with stress and strain analysis, it has the potential to unveil the effects of swelling on the structural properties of the EWPs, providing valuable knowledge for practical applications.

6 Authorship Contribution Statement

Patrick Grant: Methodology, Software, Writing - Original Draft, Writing - Review and Editing, Visualisation, Project Administration, Validation, Formal Analysis, Investigation. **Steven Psaltis** Conceptualisation, Methodology, Supervision, Writing - Review and Editing, Project Administration, Formal Analysis. **Maryam Shirmohammadi** Conceptualisation, Supervision, Writing - Review and Editing, Resources, Project Administration. **Ian Turner:** Conceptualisation, Methodology, Supervision, Writing - Review and Editing, Project Administration, Formal Analysis.

7 Declaration of Competing Interest

The authors declare that they have no known competing financial interests or personal relationships that could have appeared to influence the work reported in this paper.

8 Acknowledgements

The authors would like to acknowledge the Queensland Department of Agriculture and Fisheries, Forest Product Innovation team for supporting the experimental and imaging component of the work. This research was supported by a Queensland University of Technology Postgraduate Research Award which provided Patrick Grant with a stipend during his Doctor of Philosophy candidature.

Appendix A Iterations of Pith Location Algorithm

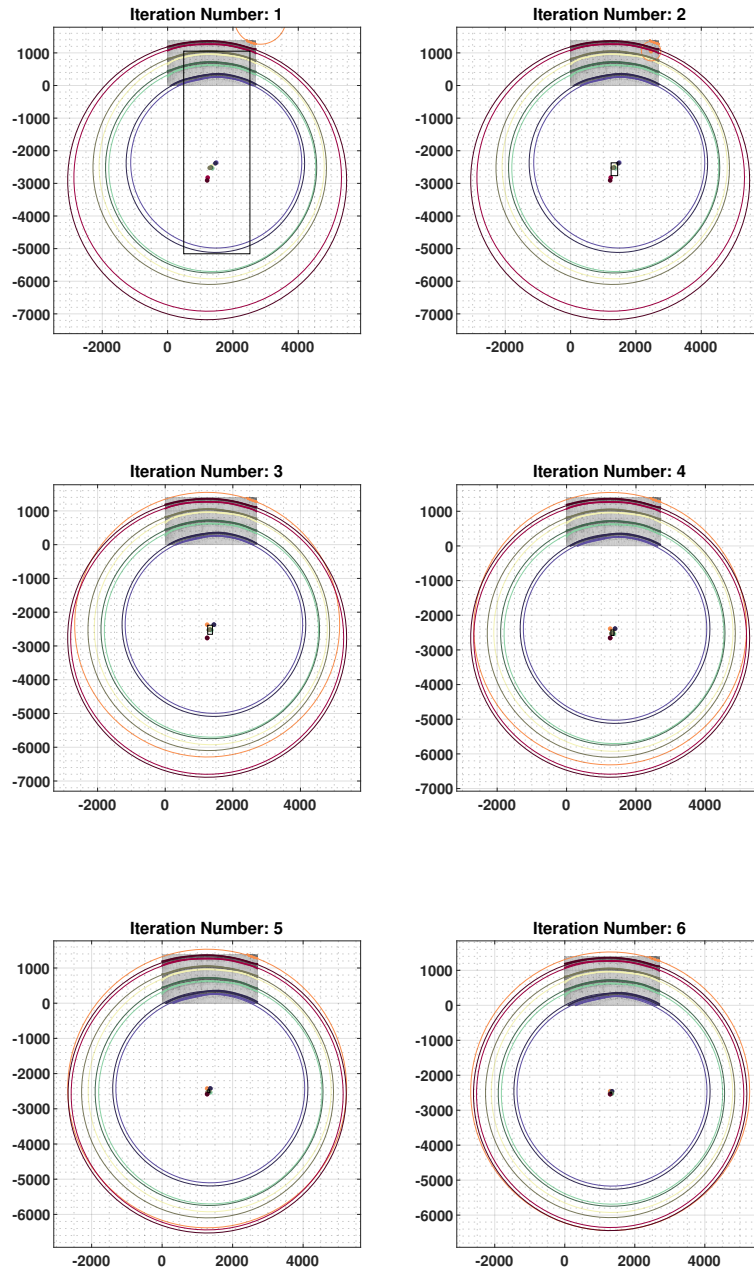


Fig. A1: Six iterations of pith location algorithm.

Appendix B Validation of the Pith Location Algorithm

To evaluate the accuracy of the pith location algorithm, we conducted a validation study on three virtual cuts made within the log. The methodology, as described in Section 2.6, was applied to these three sections, which are presented in Figure B2. The algorithm determined the pith location at approximately 16 mm, 12 mm, and 6 mm away from the true pith for the blue, purple, and red boards, respectively. While the image quality was not sufficient to obtain a suitable image mask, the latewood rings in each board were manually blacked out to provide a luminance of 0 in that pixel. It is worth noting that this masking procedure did not affect the validation of the pith location algorithm, which was the main focus of this investigation.

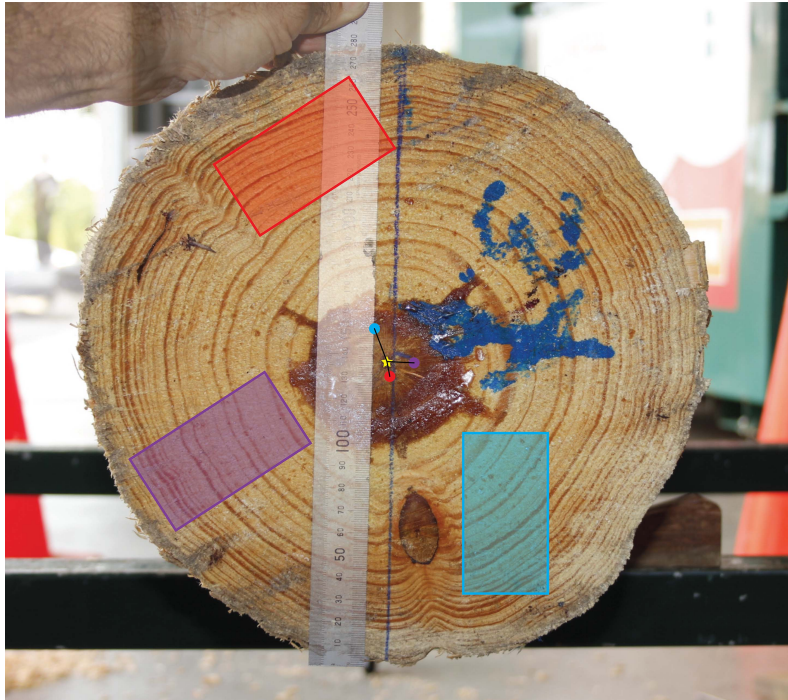


Fig. B2: The pith location algorithm tested on three sections of a swan log of radiata pine of approximately 28cm diameter. The coloured regions indicate the three different virtual cuts and the associated circle shows where the algorithm places the points where the yellow star is the true pith location. Image courtesy of Queensland Department of Agriculture and Fisheries (QDAF).

References

- Abed J, Rayburg S, Rodwell J, et al (2022) A Review of the Performance and Benefits of Mass Timber as an Alternative to Concrete and Steel for Improving the Sustainability of Structures. *Sustainability* 14(9):5570. <https://doi.org/10.3390/su14095570>
- Briggert A, Olsson A, Oscarsson J (2016) Three-Dimensional Modelling of Knots and Pith Location in Norway Spruce Boards Using Tracheid-Effect Scanning. *European Journal of Wood and Wood Products* 74:725–739. <https://doi.org/10.1007/>

s00107-016-1049-7

- Burden RL, Faires JD, Burden AM (2015) Numerical analysis. Cengage learning, Boston
- Burridge H, et al (2021) Identifying Efficient Transport Pathways in Early Wood Timber Insights From 3 D X Ray Ct Imaging of Softwood in the Presence of Flow. *Transport in Porous Media* 136(3):813–830. <https://doi.org/10.1007/s11242-020-01540-8>
- Carr EJ, Turner IW, Perre P (2011) A new control-volume finite-element scheme for heterogeneous porous media: Application to the drying of softwood. *Chemical engineering & technology* 34(7):1143–1150. <https://doi.org/10.1002/ceat.201100060>
- Cour T, Benezit F, Shi J (2005) Spectral Segmentation With Multiscale Graph Decomposition. In: 2005 IEEE Computer Society Conference on Computer Vision and Pattern Recognition (CVPR'05), IEEE, pp 1124–1131, <https://doi.org/10.1109/CVPR.2005.332>
- De Boor C, De Boor C (1978) A practical guide to splines, vol 27. Springer-Verlag, New York
- Dehariya VK, Shrivastava SK, Jain R (2010) Clustering of Image Data Set Using K Means and Fuzzy K Means Algorithms. In: 2010 International conference on computational intelligence and communication networks, IEEE, pp 386–391, <https://doi.org/10.1109/cicn.2010.80>
- Downham R, Gavran M (2019) Australian Plantation Statistics 2019 Update. Aust Gov Dep Agric Water Resour Canberra, Aust 12

- Edelsbrunner H, Mücke EP (1994) Three-dimensional alpha shapes. *ACM Transactions on Graphics (TOG)* 13(1):43–72. <https://doi.org/https://doi.org/10.1145/174462.156635>
- Fang Q, Boas DA (2009) Tetrahedral Mesh Generation From Volumetric Binary and Grayscale Images. In: 2009 IEEE international symposium on biomedical imaging: from nano to macro, Ieee, pp 1142–1145, <https://doi.org/10.1109/isbi.2009.5193259>
- Gauch JM (1999) Image Segmentation and Analysis Via Multiscale Gradient Watershed Hierarchies. *IEEE transactions on image processing* 8(1):69–79. <https://doi.org/10.1109/83.736688>
- Geuzaine C, Remacle JF (2009) Gmsh a 3D Finite Element Mesh Generator With Built in Pre and Post Processing Facilities. *International journal for numerical methods in engineering* 79(11):1309–1331. <https://doi.org/10.1002/nme.2579>
- Gevers T, Van De Weijer J, Stokman H (2006) Color Feature Detection. <https://doi.org/10.1201/9781420009781.ch9>
- Habite T, Olsson A, Oscarsson J (2020) Automatic detection of pith location along norway spruce timber boards on the basis of optical scanning. *European Journal of Wood and Wood Products* 78(6):1061–1074. <https://doi.org/10.1007/s00107-020-01558-1>
- Habite T, Abdeljaber O, Olsson A (2022) Determination of Pith Location Along Norway Spruce Timber Boards Using One Dimensional Convolutional Neural Networks Trained on Virtual Timber Boards. *Construction and Building Materials* 329:127129. <https://doi.org/10.1016/j.conbuildmat.2022.127129>
- Jia H, Ding S, Xu X, et al (2014) The Latest Research Progress on Spectral Clustering. *Neural Computing and Applications* 24:1477–1486. <https://doi.org/10.1007/>

s00521-013-1439-2

- Kadas M (2016) Greyscale-Density Calibration of an Industrial CT Scanner for Wood Microdensitometry. PhD thesis, Stellenbosch: Stellenbosch University
- Kong F, et al (2021) A deep-learning approach for direct whole-heart mesh reconstruction. *Medical image analysis* 74:102222. <https://doi.org/10.1016/j.media.2021.102222>
- Koya PR, Goshu AT (2013) Generalized mathematical model for biological growths. *Open Journal of modelling and Simulation* 2013. <https://doi.org/10.4236/ojmsi.2013.14008>
- Lazarescu C, et al (2010) Density and moisture profile evolution during timber drying by ct scanning measurements. *Drying technology* 28(4):460–467. <https://doi.org/10.1080/07373931003613478>
- Liu D, Soran B, Petrie G, et al (2012) A Review of Computer Vision Segmentation Algorithms. *Lecture notes* 53
- Liu L, Jia Z, Yang J, et al (2015) A Medical Image Enhancement Method Using Adaptive Thresholding in Nset Domain Combined Unsharp Masking. *International Journal of Imaging Systems and Technology* 25(3):199–205. <https://doi.org/10.1002/ima.22137>
- Mathworks, Inc. (2022) MATLAB Function Reference R2022a, The Mathworks, Inc., Natick, Massachusetts, p 943. Boundary
- Meilă M, Shi J (2001) A Random Walks View of Spectral Segmentation. In: *International Workshop on Artificial Intelligence and Statistics*, PMLR, pp 203–208

- Navaratnam S, Humphreys M, Mendis P, et al (2020) Effect of roof to wall connection stiffness variations on the load sharing and hold-down forces of Australian timber-framed houses. In: Structures, Elsevier, pp 141–150, <https://doi.org/10.1016/j.istruc.2020.05.040>
- Neittaanmäki P, et al (2004) Image Based Unstructured 3d Mesh Generation for Medical Applications. In: European Congress on Computational Methods in Applied Sciences and Engineering (ECCOMAS)
- Perré P (1997) Image analysis, homogenization, numerical simulation and experiment as complementary tools to enlighten the relationship between wood anatomy and drying behavior. Drying technology 15(9):2211–2238. <https://doi.org/10.1080/07373939708917359>
- Perré P (2005) Mesh Pore a Software Able to Apply Image Based Meshing Techniques to Anisotropic and Heterogeneous Porous Media. Drying technology 23(9-11):1993–2006. <https://doi.org/10.1080/07373930500210432>
- Perré P, Turner I (2001) Determination of the Material Property Variations Across the Growth Ring of Softwood for Use in a Heterogeneous Drying Model Part 1 Capillary Pressure Tracheid Model and Absolute Permeability. Wood Research and Technology <https://doi.org/10.1515/hf.2001.052>
- Perre P, Turner I (2002) A heterogeneous wood drying computational model that accounts for material property variation across growth rings. Chemical Engineering Journal 86(1-2):117–131. [https://doi.org/https://doi.org/10.1016/S1385-8947\(01\)00270-4](https://doi.org/https://doi.org/10.1016/S1385-8947(01)00270-4)
- Psaltis S, Kumar C, Turner I, et al (2021) A new approach for predicting board MOE from increment cores. Annals of Forest Science 78(3):1–16. <https://doi.org/10.1007/>

s13595-021-01093-w

- Reinsch CH (1967) Smoothing by spline functions. *Numerische mathematik* 10(3):177–183. <https://doi.org/10.1007/bf02162161>
- Shrivakshan G, Chandrasekar C (2012) A Comparison of Various Edge Detection Techniques Used in Image Processing. *International Journal of Computer Science Issues (IJCSI)* 9(5):269
- Siau JF (1984) *Transport Processes in Wood*. Springer Series in Wood Science ; v. 2, Springer-Verlag, Berlin
- Stamm AJ (1961) Comparison Between Measured and Theoretical Drying Diffusion Coefficients Southern Pine. *for Prod J* 11:536–543
- The Mathworks, Inc. (2022a) MATLAB. <https://au.mathworks.com/products/matlab.html>
- The Mathworks, Inc. (2022b) MATLAB: Curve Fitting Toolbox. <https://au.mathworks.com/products/curvefitting.html?requestedDomain=>
- Thomas D, Ding G (2018) Comparing the Performance of Brick and Timber in Residential Buildings - The Case of Australia. *Energy and buildings* 159:136–147. <https://doi.org/10.1016/j.enbuild.2017.10.094>
- Von Luxburg U (2007) A tutorial on spectral clustering. *Statistics and computing* 17(4):395–416. <https://doi.org/10.1007/s11222-007-9033-z>
- Wood Solutions (2022) 25 King St. [Online; accessed 22/08/2022]. <https://www.woodsolutions.com.au/case-studies/25-king-st>